Article

High-Moment FeCo Magnetic Nanoparticles Obtained by Topochemical H₂ Reduction of Co-Ferrites

Alexander Omelyanchik [1,2], Gaspare Varvaro [3], Pierfrancesco Maltoni [4], Valeria Rodionova [2], Jean-Pierre Miranda Murillo [1], Federico Locardi [1], Maurizio Ferretti [1], Claudio Sangregorio [5], Fabio Canepa [1], Petr Chernavsky [6], Nikolai Perov [7] and Davide Peddis [1,3,*]

1 Department of Chemistry and Industrial Chemistry, University of Genova, 16146 Genova, Italy; asomelyanchik@kantiana.ru (A.O.); jean_genoa96@live.it (J.-P.M.M.); federico.locardi@unige.it (F.L.); ferretti@chimica.unige.it (M.F.); fabio.canepa@unige.it (F.C.)
2 REC "Smart Materials and Biomedical Applications", Immanuel Kant Baltic Federal University, 236041 Kaliningrad, Russia; valeriarodionova@gmail.com
3 Consiglio Nazionale delle Ricerche, nM²-Lab, Istituto di Struttura della Materia, Monterotondo Scalo, 00015 Rome, Italy; gaspare.varvaro@ism.cnr.it
4 Department of Materials Science and Engineering, Uppsala University, P.O. Box 35, SE-751 03 Uppsala, Sweden; pierfrancesco.maltoni@angstrom.uu.se
5 Istituto di Chimica dei Composti OrganoMetallici & INSTM, 50019 Sesto Fiorentino, Italy; csangregorio@iccom.cnr.it
6 Chemical Department, Lomonosov Moscow State University, 119991 Moscow, Russia; chern5@inbox.ru
7 Faculty of Physics, Lomonosov Moscow State University, 119991 Moscow, Russia; perov@magn.ru
* Correspondence: davide.peddis@unige.it

Featured Application: Metallic nanoparticles with a high value of magnetization have potential interest for application in biomedicine, catalysis, composite permanent magnets, and other fields.

Abstract: Cobalt ferrite nanoparticles of different stoichiometries synthesized by a sol–gel autocombustion method were used as a starting material to obtain high-moment $Fe_{50}Co_{50}$ and $Fe_{66}Co_{34}$ metal nanoparticles by topochemical hydrogen reduction. Structural and magnetic investigations confirmed the formation of FeCo nanoparticles with crystallite sizes of about 30 nm and magnetization at 0.5 T of ~265 Am^2/kg (0 K), which was larger than the expected bulk value, likely because of the incorporation in the body-centered cubic (bcc) FeCo structure of the residual C atoms present on the surface of the oxide particles. Temperature-dependent magnetization measurements in the H_2 atmosphere were also performed to investigate in detail the reduction mechanism and the effect of an external magnetic field on the process efficiency.

Keywords: magnetic nanoparticles; metal nanoparticles; hydrogen reduction; magnetic materials

1. Introduction

High-magnetic-moment nanoparticles (MNPs), such as metallic Fe, Co, α″-$Fe_{16}N_2$, and FeCo(Ni) binary alloys, have been the subject of intense research activity, owing to their potential applications in many different fields [1–8] exploiting their high saturation magnetization (M_S) which exceed by a factor of two or more the typical values of oxide materials (e.g., Fe_3O_4 and $CoFe_2O_4$) [5]. A high magnetic moment is strongly desired for theranostic applications, as it leads to (1) a more efficient manipulation of magnetic particles by an external magnetic field and (2) higher contrast in magnetic particle or magnetic resonance imaging and more efficient heat generation in hyperthermia treatments [9]. However, different from oxide materials, metallic nanoparticles can be toxic, owing to their strong reactivity with oxygen, and they must be covered with a biocompatible shell, such as carbon [9–11], SiO_2 [12], or Au [13]. On the other hand, in a non-oxidizing environment, the chemical activity of zero-valent metallic particles can be exploited to catalyze specific

reactions. For example, the catalytic activity of Fe and Co is crucially important in hydrocarbon synthesis in the Fischer–Tropsch process [14], and the use of nanoparticles with a high surface-to-volume ratio enhances the rate of this reaction [4]. Additionally, in combination with magnetically hard materials, soft MNPs with a high magnetic moment can be used as building blocks of rare-earth-free nanostructured permanent magnets which match or surpass the performance of current permanent magnets containing critical rare-earth elements [15,16]. Within this framework, Granados-Miralles et al. recently showed that it is possible to regulate the degree of reduction of cobalt ferrite MNPs to optimize the magnetic coupling with FeCo phases as a novel approach toward permanent magnets [17].

Among the family members, the $Fe_{100-x}Co_x$ intermetallic alloys show a distinctive combination of a high Curie temperature, low magneto-crystalline anisotropy, and high saturation magnetization, which reaches a maximum value of 240 Am^2/kg in the $Fe_{65}Co_{35}$ alloy [18–20]. Despite these interesting properties, FeCo particles are unstable in air and relatively difficult to synthesize with respect to magnetic oxide materials [21]. Several techniques have been proposed to synthesize pure FeCo alloy nanoparticles, including physical vapor nanoparticle deposition [13,22], methane chemical vapor deposition [9,10], and polyol methods [23,24]. However, it is still challenging to find a large-scale, efficient, and low-cost method for their fabrication. A promising strategy, which was already applied to synthesize high-moment and air-stable α-Fe MNPs [25], implies the use of oxide-based MNPs and their reduction in the H_2 atmosphere. Despite this method, referred to as hydrogen reduction, being widely used to produce bulk metals due to its industrial importance in metallurgy [26], its implementation in nanoparticle synthesis is more difficult, owing to the higher cost of the parent nanoparticle materials and the increase in particle size at high temperatures [4,25]. In this regard, a bigger effort may be put forth to develop an easy and scalable way to synthesize oxide precursors with high-quality nanocrystallites to preserve the nanoscale features before undergoing reduction [27,28]. Moreover, to make the process more efficient, different strategies have been proposed, such as the use of hydrogen at high pressure [29] or the application of a magnetic field during the reaction [30,31]. The latter was demonstrated to be highly efficient in terms of reduction of the processing temperature. However, the effect of an external magnetic field on the topochemical reduction process is still under discussion, and further studies are necessary to better disclose and control the process.

In this work, high-moment $Fe_{50}Co_{50}$ and $Fe_{66}Co_{34}$ MNPs were synthesized by hydrogen reduction of stoichiometric and non-stoichiometric Co-ferrite MNPs obtained via the sol–gel autocombustion method, which is a relatively simple, eco-friendly, and cheap strategy allowing one to produce the spinel ferrite MNPs [32,33]. Moreover, the obtained powder shows an extremely high porosity [32], providing a high interface between solid and gaseous phases that favors heterogeneous reactions, such as topochemical H_2 reduction. X-ray diffraction (XRD), differential thermal analysis and thermogravimetry (DTA/TG), and superconducting quantum interference device (SQUID) magnetometry were combined to deeply investigate the correlation between the magnetic and morpho-structural properties of both the metallic and starting oxide particles. Moreover, the reduction kinetics and the effect of an external magnetic field applied during the process were carefully investigated by recording the temperature dependence of the magnetization during the H_2 reduction of oxide particles.

2. Materials and Methods

2.1. Synthesis of Co-Ferrite Nanoparticles

Co-ferrite nanoparticles with a Co:Fe ratio of 2:1 and 1:1 were prepared by the sol–gel autocombustion method. This method of synthesis has been previously used to obtain cobalt ferrite and doped cobalt ferrite nanoparticles [28,32–34]. $Fe(NO_3)_3 \cdot 9H_2O$ ($\geq$98%, Sigma-Aldrich) and $Co(NO_3)_2 \cdot 6H_2O$ (Scharlab S.L., Barcelona, Spain) metal salts were first dissolved in distilled water. The molar ratio between Fe and Co was set to 2:1 and 1:1 to obtain FeCo particles with different compositions (i.e., $Fe_{50}Co_{50}$ and $Fe_{66}Co_{34}$) after H_2

reduction (see the next section). Then, 1-molar solution of the citric acid ($\geq$99.5, Carlo Erba Reagenti SpA) was added to set 1:1 molarity with the metal salts. The pH level was adjusted to 7 by dropwise adding of 28–30% ammonia solution (Sigma-Aldrich, St. Louis, MO, USA). The obtained sol was dried for about 120 min at 150 °C to form a gel. The self-combustion reaction was induced by an increase in temperature up to 300 °C. The obtained powders were finally collected and grinded with an agate mortar.

2.2. H₂ Reduction of Co-Ferrite Nanoparticles

Oxide MNPs were placed in an alumina boat crucible and inserted into a quartz tube inside a tubular furnace. The tube was heated at 200 °C (2 h) in an N_2 flow (50 mL/min) to remove moisture and air. The reduction was performed at 500 °C (5 h) in a dynamic flow of the mixture of H_2 (50 mL/min) and N_2 (20 mL/min). After reduction, the samples were passivated in the N_2 atmosphere during overnight cooling and transferred into an inert glove box workstation (MBRAUN) with an N_2 atmosphere ($H_2O < 0.3$ ppm; $O_2 < 0.1$ ppm).

2.3. Samples' Characterization

Phase identification and structural characterization were performed by means of a MiniFlex (Rigaku) X-ray diffractometer (XRD) using a Cu Kα anode (λ = 1.54184 Å) in the 2θ geometry. Analysis of the XRD patterns was performed with Maud software. The crystallographic information files (.cif) were acquired from the crystallographic open database (COD) [35]. The size of the crystallites (d_{XRD}) and the lattice parameter (*a*) were calculated by using the Scherrer formula while considering crystallites with spherical shapes [36,37].

Differential thermal analysis and thermogravimetry (DTA/TG) were performed by using a LabsysEvo 1600 DTA/TGA (Setaram). About 5 mg of the sample obtained after reduction were put in an alumina crucible and heated from 30 to 1000 °C at 10 °C/min under an O_2 or Ar atmosphere (20 mL/min).

Field-dependent magnetization loops were measured by using a Quantum Design SQUID magnetometer in the field range $\pm$5 T at 5 K and 300 K. Samples were prepared in an N_2 atmosphere inside the glove box and closed by glue to prevent particle contact with ambient oxygen.

## 2.4. In Situ Study of the Reduction Kinetics

The reduction kinetics was investigated by recording the temperature dependence of the magnetization during the H_2 reduction of the oxide particles [31,38]. The samples (~10 mg) were placed in a measuring cell of a vibrating sample magnetometer (VSM, built in house [38]), consisting of a flow-through microreactor with an internal volume of 0.3 cm^3. The samples were clamped between two membranes of porous quartz.

The samples were heated in an Ar flow (30 mL/min) of up to 200 °C at a heating rate of 9 °C/min., and then the temperature was kept constant until a stable magnetization value was reached. The magnetization was measured at a frequency of 1 Hz. The same measurement was then performed by replacing the Ar flow with H_2 (flow 30 mL/min) and gradually increasing the temperature up to 500 °C at a heating rate of 9 °C/min.

3. Results

The XRD patterns of the Co-ferrite particles (Figure 1) confirmed the formation of a phase-pure cubic spinel structure for both samples (COD card no. 1,533,163 [39]). When the Fe:Co molar ratio of the starting salts was set to 2:1 with the stoichiometry $CoFe_2O_4$ nanoparticles form, while a mixture of $CoFe_2O_4$ and $FeCo_2O_4$ phases was likely obtained when the Fe:Co ratio was set to 1:1 [40]. Hereafter, we will use the conditional formula "$(CoFe)_3O_4$" to indicate the latter sample. In stoichiometric $CoFe_2O_4$, Co^{2+} cations preferentially occupy octahedral sites with an inversion degree of ~0.8. In cobalt-rich spinel ferrites, some cobalt ions are in the 3+ low-spin state and preferentially occupy the octahedral sites, pushing some Co^{2+} to tetrahedral positions and thus reducing the inversion degree toward

~0.5 [40]. As a result, the lattice parameter *a* decreased from 0.8381(1) nm for $CoFe_2O_4$ to 0.8242 (2) nm for $FeCo_2O_4$ [40], and the reflection peaks of the Co-reach spinel ferrites shifted to higher 2θ values. In our samples, the lattice parameter of the stoichiometric sample was 0.8392(5) nm, which was very close to the nominal value, and it decreased to 0.8346(6) nm for the $(CoFe)_3O_4$ sample, thus confirming the trend of reduction of the lattice parameter while increasing the Co percentage.
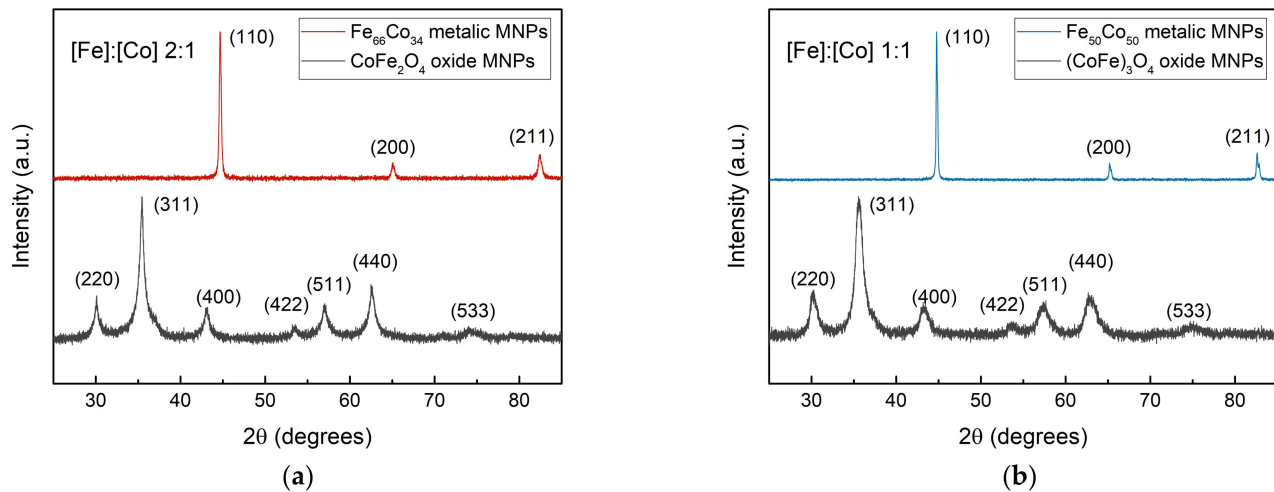
**Figure 1.** XRD patterns of (**a**) $CoFe_2O_4$ and corresponding metallic $Fe_{66}Co_{34}$ MNPs and (**b**) $(CoFe)_3O_4$ and corresponding metallic $Fe_{50}Co_{50}$ MNPs. Diffraction peaks of oxide and reduced powders are indexed by cubic spinel ferrite and body-centered cubic (bcc) FeCo phase, respectively (the corresponding Miller indexes are reported).

The crystallite size (d_{XRD}) estimated using Scherrer's equation [37] was ~12 and 7 nm for the $CoFe_2O_4$ and $(CoFe)_3O_4$ particles, respectively. The XRD patterns of the samples after H_2 reduction featured drastic changes in the position and width of the diffraction peaks, which could be indexed to the bcc FeCo phase (I m -3 m structure, COD card no. 1100108). Lattice parameters of 0.2866(1) nm and 0.2859(7) nm, indicating the formation of $Fe_{66}Co_{34}$ and $Fe_{50}Co_{50}$ MNPs were estimated for the FeCo particles obtained from $CoFe_2O_4$ and $(CoFe)_3O_4$ oxides, respectively. Moreover, it is worth noting that the size of the crystallites increased up to 25 nm and 33 nm for the $Fe_{66}Co_{34}$ and $Fe_{50}Co_{50}$ samples, respectively.

The magnetic properties confirmed the change of the particle structure after H_2 reduction (Figure 2 and Table 1). At low temperatures (5 K), the $CoFe_2O_4$ and $(CoFe)_3O_4$ samples possessed a large coercivity (H_C), resulting from the high magnetic anisotropy of Co-ferrites, and a saturation magnetization (M_S) lower than the bulk value (90 Am^2/kg for stoichiometric cobalt ferrite at 0 K [41]), owing to the large contribution of magnetically frustrated surface spins in small nanoparticles [28,42,43]. The coercivity rapidly reduced when measurements were performed at 300 K, due to thermal fluctuation occurring when the temperature approached the blocking temperature (T_B, which was above room temperature for those samples) according to the following equation:

$$H_C(T) = \zeta \frac{2K}{M_S} \left[1 - \left(\frac{T}{T_B} \right)^{\frac{1}{2}} \right], \tag{1}$$

where *K* is the magnetic anisotropy constant and ζ is a coefficient that mainly depends on the anisotropy symmetry [44].
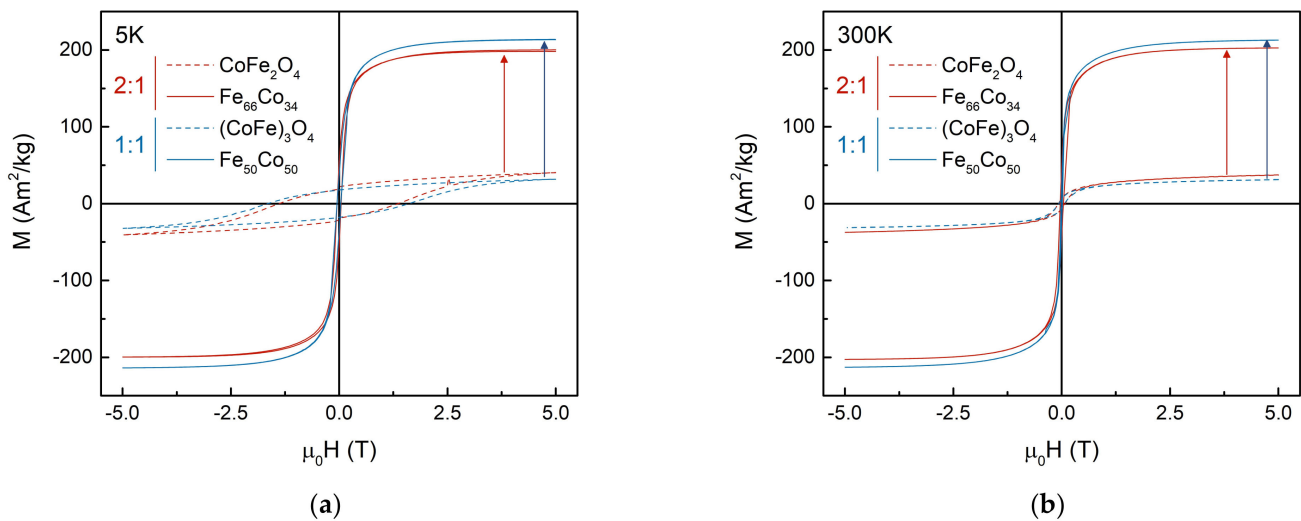
Figure 2. Field dependence of magnetization of oxide and metallic MNPs measured at (**a**) 5 K and (**b**) 300 K.

Table 1. Structural and magnetic properties of Co-ferrite and corresponding FeCo metal MNPs. Uncertainties on the last digit are given in parentheses.

Sample:		$CoFe_2O_4$	$Fe_{66}Co_{34}$	$(CoFe)_3O_4$	$Fe_{50}Co_{50}$
space group		F d −3 m	I m −3 m	F d −3 m	I m −3 m
a, nm		0.8392(5)	0.2866(1)	0.8346(6)	0.2859(7)
d_{XRD}, nm		12(1)	25(6)	7(1)	33(8)
M_S, Am^2/kg	5 K	54(2)	199(4)	41(2)	215(4)
	300 K	45(2)	203(4)	35(2)	215(4)
μ_0H_C, T	5 K	1.37(2)	0.045(3)	1.63(3)	0.042(6)
	300 K	0.073(2)	0.039(1)	0.068(2)	0.012(2)
M_R/M_S	5 K	0.37(4)	0.25(2)	0.44(4)	0.16(2)
	300 K	0.14(2)	0.21(2)	0.16(2)	0.12(2)
$T_{oxidation}$, °C		—	410(4)	—	453(2) 496(4)
$T_{reduction}$, °C	μ_0H = 10 mT	349(5)	—	357(5)	—
	μ_0H = 0.5 T	328(5)		333(5)	

The M-H loops for both H_2-reduced samples were characterized by an increased M_S and reduced H_C. The saturation magnetization at 5 K reached values of ~203 Am^2/kg and ~215 Am^2/kg for the $Fe_{50}Co_{50}$ and $Fe_{66}Co_{34}$ MNPs, respectively, which were slightly lower than the values of FeCo bulk alloys of similar compositions [20]. This reduction was probably due to the formation of a thin oxide shell, which may have arisen at the intermediate step when the sample was transferred from the furnace to the glow box. Additionally, the magnetic properties of both metallic MNPs were much less temperature-dependent because of the higher size of these particles compared with the oxide ones.

To additionally prove the effectiveness of the reduction, the reverse mechanism (i.e., the oxidation of metallic MNPs) was investigated by performing DTA/TG in an O_2 atmosphere (Figure 3). The mass gain during oxidation for both samples was ~36%, consistent with the value expected from the difference between the molar mass (M_W) of $Fe_{66}Co_{34}$ (~171 g/mol) and $CoFe_2O_4$ (~235 g/mol) (i.e., ($M_W[CoFe_2O_4]/M_W[Fe_{66}Co_{34}]$ − 1) × 100% = 37.5%). A similar value of 37.2% was measured for the $Fe_{50}Co_{50}$ sample. Oxidation of the $Fe_{66}Co_{34}$ sample occurred in a single step at a temperature of ~410 °C (exothermic peak of DTA curve), while the oxidation of the $Fe_{50}Co_{50}$ MNPs occurred at higher temperatures [45], and it had a two-step character. This may have been due to the heterogeneity of the starting

material, which may have contained two different oxide phases. TG measurements of the $Fe_{50}Co_{50}$ MNPs under an inert atmosphere (Ar) showed no significant mass variations. The DTA clearly revealed the bcc (α-phase) to fcc (γ-phase) transition (endothermal peak at ~982 °C). According to the Fe-Co phase diagram, the position of this peak depended on the alloy composition and, for the $Fe_{55}Co_{45}$ composition, reached a maximum value of ~985 °C [46]. The sharpness of the peak indirectly indicated the compositional homogeneity of the $Fe_{50}Co_{50}$ sample, despite the suspicion of the heterogeneity of the parent oxide sample $(CoFe)_3O_4$. It is also interesting to note that after oxidation at 1000 °C, the size of the crystallites, evaluated from the XRD pattern, remained almost unchanged compared with the metallic particles.
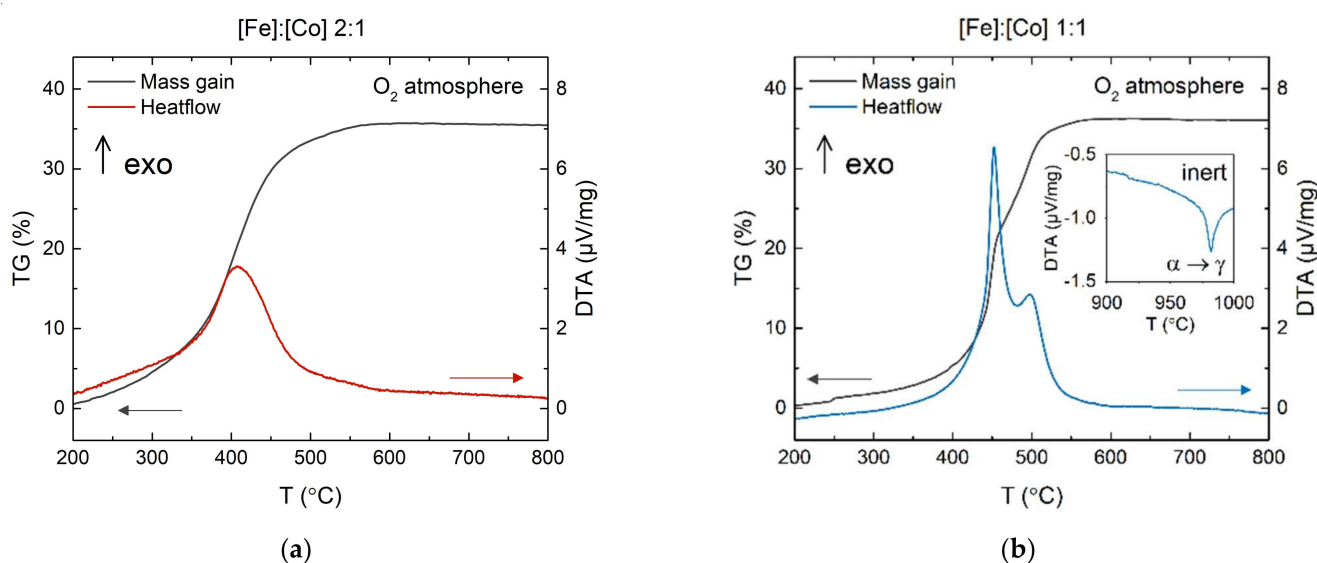
Figure 3. DTA (red or blue) and TG (black) curves recorded in the O_2 atmosphere for (**a**) $Fe_{66}Co_{34}$ and (**b**) $Fe_{50}Co_{50}$ MNPs. The inset of (**b**) is the DTA curve of the $Fe_{50}Co_{50}$ MNPs measured in an Ar atmosphere.

To study in detail the reduction process and the effect of an external magnetic field, the temperature dependence of the magnetization was measured during the reduction of Co-ferrite powders under a reductive H_2 atmosphere (Figure 4). Magnetization was recorded as a function of the temperature under a magnetic field of 10 mT and 0.5 T. Since the magnetic properties of the Co-ferrite oxides and FeCo metals were very different, the sudden increase in magnetization around ~350 °C may have been associated with the reduction of oxides to metals. The rate of reduction process could be estimated from the derivative of magnetization versus temperature dM(T)/dT. The maxima of these curves depended on the applied magnetic field. In the higher field, this peak shifted toward a lower temperature of about 20–25 °C, thus suggesting that the magnetic field promoted the reduction process.

Moreover, analysis of the M(T) curves recorded during reduction allowed for disclosing the topochemical reaction mechanisms. It was recently demonstrated that the reduction of Fe_3O_4 particles in H_2 can occur in one- or two-step processes [31], the latter being due to the formation of an intermediate antiferromagnetic FeO phase (paramagnetic above the Néel temperature T_N = 198 K [41]). In the case of Co-ferrites, in a hypothetical two-step process, the Me_3O_4 spinel phase (where $Me^{2+/3+}$ is a $Fe^{2+/3+}$ or $Co^{2+/3+}$ metal ion) may first transform to a MeO rock salt phase and finally to a pure Me phase. In a one-step process, the Co ferrites directly transform to a pure metal phase. Since, in both samples, no significant change in magnetization was detected after the sudden increase of the moment, one can conclude that the mechanism of the topochemical process occurred in one step in both the low and high magnetic fields, or a two-step process occurred smoothly at the same temperature.
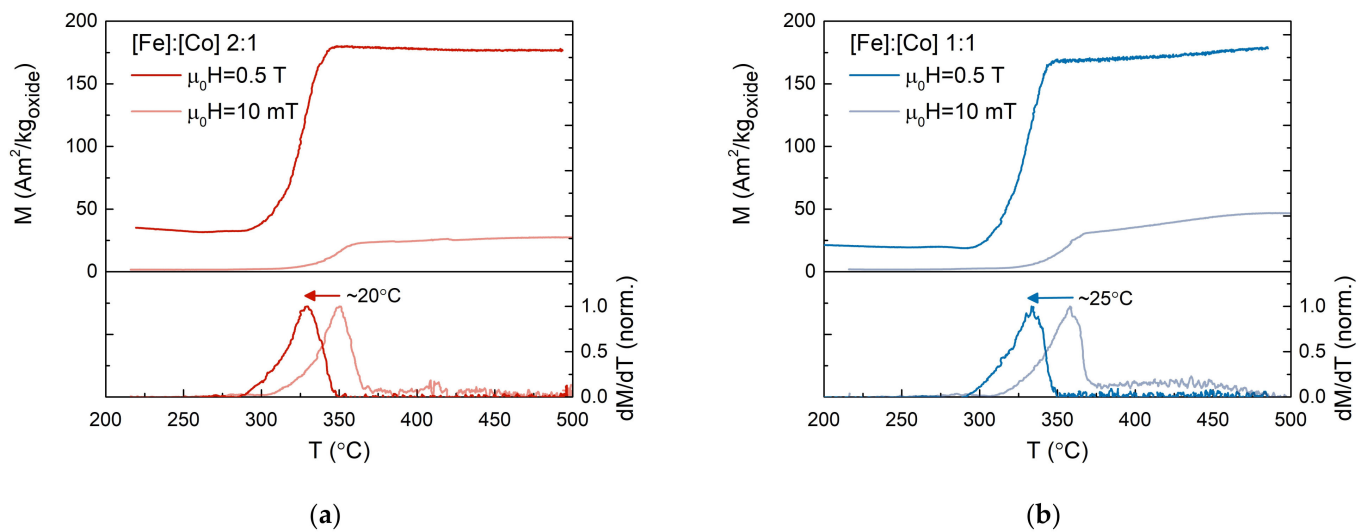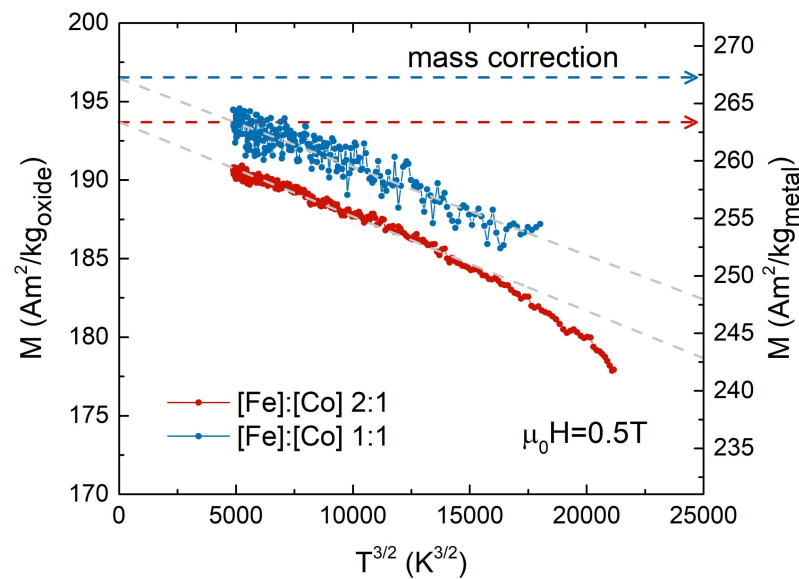
Figure 4. Temperature dependence of magnetization under an external magnetic field of 10 mT and 0.5 T, measured during the H_2 reduction of (**a**) $CoFe_2O_4$ and (**b**) $(CoFe)_3O_4$ MNPs. Bottom panels: normalized first derivative of magnetization vs. temperature curve.

After the samples were reduced, the M(T) curves were recorded during cooling (Figure 5). Considering that at a field of 0.5 T the system was close to the saturation state, and the studied temperature range was still relatively far from the Curie temperatures ($T_C(Fe_{67}Co_{33})$ = 985 °C, $T_C(Fe_{51}Co_{49})$ = 964 °C [24]), Bloch's law could be applied to describe the reduction in magnetization:

$$M(T) = M_0\left(1 - BT^\beta\right),\tag{2}$$

where B is the Bloch constant, β is the Bloch exponent (which is usually in the range of 1.5–2), and M_0 is the magnetization at 0 K [47,48]. By fitting the low-temperature region of the experimental curves reported in the $T^{3/2}$ scale, the magnetization at 0 K (M_0) was estimated to be 263 ± 2 Am^2/kg and 267 ± 4 Am^2/kg for the $Fe_{66}Co_{34}$ and $Fe_{50}Co_{50}$ samples, respectively. It is worth mentioning that these values were obtained after correcting the mass for the losses measured during the reduction process (see the section with TGA). The M_0 values were significantly higher than the saturation magnetization determined by SQUID measurements, probably because in this latter case, the samples were partially oxidized during the quick exposition to air before SQUID measurements. Moreover, the estimated M_0 values were significantly higher than those expected for bulk materials (more than about 20% because at 0.5 T, the saturation was not completely reached). Similar to what was already observed in the α-Fe particles obtained after high-pressure hydrogenation treatments [25], the enhancement of the saturation magnetization may be explained by the local changes of the electronic configurations due to the incorporation into the bcc FeCo structure of residual C atoms present on the surface of the oxide particles after the combustion of citric acid. Further investigations of this issue should be conducted with a wide range of samples.

Figure 5. Temperature dependence of the magnetization measured during cooling under a magnetic field of 0.5 T for as-reduced $Fe_{66}Co_{34}$ and $Fe_{50}Co_{50}$ MNPs. (left axis) M is the magnetic moment divided by the mass of initial oxide powder (m_{oxide}). (right axis) M is the magnetic moment divided by the mass of derived metal $m_{metal} = m_{oxide} \times (M_w^{oxide}/M_w^{metal})$.

4. Conclusions

High-moment FeCo nanoparticles with tunable compositions can be easily obtained by topochemical H_2 reduction (~350 °C) of Co-ferrite nanoparticles with different Fe/Co ratios. Both structural and magnetic characterizations confirmed the formation of metallic FeCo alloy nanoparticles with an average crystallite size of ~30 nm featured by a high magnetization (~265 Am^2/kg at 0 K and 0.5 T), significantly larger than the values of the FeCo bulk alloys of similar compositions, which could be ascribed to the presence of C atoms in the crystal structure coming from residual carbon present on the surface of the oxide particles. Temperature-dependent magnetization measurements indicate that the reduction of Co-ferrite to FeCo nanoparticles is a one-step process whose efficiency in terms of reduction of the processing temperature can be significantly enhanced through the application of a moderate external field (0.5 T), thus paving the way for the development of sustainable syntheses of high-moment metal nanoparticles.

Author Contributions: Conceptualization, A.O. and D.P.; methodology, F.L., P.C., N.P., F.C. and D.P.; validation C.S., V.R., F.L., M.F., N.P., F.C. and D.P.; formal analysis, C.S., N.P., F.C. and D.P.; investigation, A.O., G.V., P.M., J.-P.M.M., P.C., F.C. and D.P.; resources, N.P., F.C. and D.P.; data curation, A.O. and D.P.; writing—original draft preparation, A.O.; writing—review and editing, G.V., P.M., C.S., N.P., F.C. and D.P.; visualization, A.O.; supervision, V.R., M.F., N.P., F.C. and D.P.; project administration, D.P.; funding acquisition, V.R. and D.P. All authors have read and agreed to the published version of the manuscript.

Institutional Review Board Statement: Not applicable.

Informed Consent Statement: Not applicable.

Data Availability Statement: Not applicable.

References

1. Desvaux, C.; Amiens, C.; Fejes, P.; Renaud, P.; Respaud, M.; Lecante, P.; Snoeck, E.; Chaudret, B. Multimillimetre-large superlattices of air-stable iron-cobalt nanoparticles. *Nat. Mater.* **2005**, *4*, 750–753. [CrossRef]
2. Reiss, G.; Hütten, A. Magnetic nanoparticles: Applications beyond data storage. *Nat. Mater.* **2005**, *4*, 725–726. [CrossRef]
3. Ener, S.; Anagnostopoulou, E.; Dirba, I.; Lacroix, L.M.; Ott, F.; Blon, T.; Piquemal, J.Y.; Skokov, K.P.; Gutfleisch, O.; Viau, G. Consolidation of cobalt nanorods: A new route for rare-earth free nanostructured permanent magnets. *Acta Mater.* **2018**, *145*, 290–297. [CrossRef]
4. Huber, D.L. Synthesis, properties, and applications of iron nanoparticles. *Small* **2005**, *1*, 482–501. [CrossRef] [PubMed]
5. Liu, J.; Su, D.; Wu, K.; Wang, J. High-moment magnetic nanoparticles. *J. Nanoparticle Res.* **2020**, *22*, 66. [CrossRef]
6. Farkaš, B.; De Leeuw, N.H. A perspective on modelling metallic magnetic nanoparticles in biomedicine: From monometals to nanoalloys and ligand-protected particles. *Materials* **2021**, *14*, 3611. [CrossRef] [PubMed]
7. Katz, E. Synthesis, properties and applications of magnetic nanoparticles and nanowires—A brief introduction. *Magnetochemistry* **2019**, *5*, 61. [CrossRef]
8. Folsom, S.K.; Ivey, D.J.; McNair, F.S.; Siamaki, A.R. Nickel-fe3 o4 magnetic nanoparticles supported on multiwalled carbon nanotubes: Effective catalyst in suzuki cross coupling reactions. *Catalysts* **2021**, *11*, 495. [CrossRef]
9. Song, G.; Kenney, M.; Chen, Y.-S.; Zheng, X.; Deng, Y.; Chen, Z.; Wang, S.X.; Gambhir, S.S.; Dai, H.; Rao, J. Carbon-coated FeCo nanoparticles as sensitive magnetic-particle-imaging tracers with photothermal and magnetothermal properties. *Nat. Biomed. Eng.* **2020**, *4*, 325–334. [CrossRef] [PubMed]
10. Sherlock, S.P.; Tabakman, S.M.; Xie, L.; Dai, H. Photothermally enhanced drug delivery by ultrasmall multifunctional FeCo/graphitic shell nanocrystals. *ACS Nano* **2011**, *5*, 1505–1512. [CrossRef] [PubMed]
11. Seo, W.S.; Lee, J.H.; Sun, X.; Suzuki, Y.; Mann, D.; Liu, Z.; Terashima, M.; Yang, P.C.; McConnell, M.V.; Nishimura, D.G.; et al. FeCo/graphitic-shell nanocrystals as advanced magnetic-resonance-imaging and near-infrared agents. *Nat. Mater.* **2006**, *5*, 971–976. [CrossRef] [PubMed]
12. Bai, J.; Xu, Y.H.; Thomas, J.; Wang, J.P. (FeCo)$_3$Si-SiO$_x$ core-shell nanoparticles fabricated in the gas phase. *Nanotechnology* **2007**, *18*, 065701. [CrossRef]
13. Xu, Y.H.; Bai, J.; Wang, J.P. High-magnetic-moment multifunctional nanoparticles for nanomedicine applications. *J. Magn. Magn. Mater.* **2007**, *311*, 131–134. [CrossRef]
14. Van Der Laan, G.P.; Beenackers, A.A.C.M. Kinetics and Selectivity of the Fischer-Tropsch Synthesis: A Literature Review. *Catal. Rev. Sci. Eng.* **1999**, *41*, 255–318. [CrossRef]
15. Liu, F.; Dong, Y.; Yang, W.; Yu, J.; Xu, Z.; Hou, Y. Exchange-coupled fct-FePd/α-Fe nanocomposite magnets converted from Pd/Fe3O4 core/shell nanoparticles. *Chem. A Eur. J.* **2014**, *20*, 15197–15202. [CrossRef] [PubMed]
16. Shen, B.; Sun, S. Chemical Synthesis of Magnetic Nanoparticles for Permanent Magnet Applications. *Chem. A Eur. J.* **2020**, *26*, 6757–6766. [CrossRef]
17. Granados-Miralles, C.; Quesada, A.; Saura-Múzquiz, M.; Andersen, H.L.; Fernández, J.F.; Christensen, M. Expanding the tunability and applicability of exchange-coupled/decoupled magnetic nanocomposites. *Mater. Chem. Front.* **2020**, *4*, 1222–1230. [CrossRef]
18. Sundar, R.S.; Deevi, S.C. Soft magnetic FeCo alloys: Alloy development, processing, and properties. *Int. Mater. Rev.* **2005**, *50*, 157–192. [CrossRef]
19. Bardos, D.I. Mean Magnetic Moments in bcc Fe–Co Alloys. *J. Appl. Phys.* **1969**, *40*, 1371–1372. [CrossRef]
20. Sánchez-De Jesús, F.; Bolarín-Miró, A.M.; Cortés Escobedo, C.A.; Torres-Villaseñor, G.; Vera-Serna, P. Structural Analysis and Magnetic Properties of FeCo Alloys Obtained by Mechanical Alloying. *J. Metall.* **2016**, *2016*, 1–8. [CrossRef]
21. Pervikov, A.V. Metal, Metal Composite, and Composited Nanoparticles Obtained by Electrical Explosion of Wires. *Nanobiotechnol. Rep.* **2021**, *16*, 401–420. [CrossRef]
22. Bai, J.; Wang, J.P. High-magnetic-moment core-shell-type FeCo-Au/Ag nanoparticles. *Appl. Phys. Lett.* **2005**, *87*, 1–3. [CrossRef]
23. Abbas, M.; Nazrul Islam, M.; Parvatheeswara Rao, B.; Ogawa, T.; Takahashi, M.; Kim, C. One-pot synthesis of high magnetization air-stable FeCo nanoparticles by modified polyol method. *Mater. Lett.* **2013**, *91*, 326–329. [CrossRef]
24. Karipoth, P.; Thirumurugan, A.; Justin Joseyphus, R. Synthesis and magnetic properties of flower-like FeCo particles through a one pot polyol process. *J. Colloid Interface Sci.* **2013**, *404*, 49–55. [CrossRef]
25. Greculeasa, S.G.; Palade, P.; Schinteie, G.; Leca, A.; Dumitrache, F.; Lungu, I.; Prodan, G.; Kuncser, A.; Kuncser, V. Tuning structural and magnetic properties of Fe oxide nanoparticles by specific hydrogenation treatments. *Sci. Rep.* **2020**, *10*, 1–13. [CrossRef] [PubMed]
26. Spreitzer, D.; Schenk, J. Reduction of Iron Oxides with Hydrogen—A Review. *Steel Res. Int.* **2019**, *90*, 1900108. [CrossRef]
27. Maltoni, P.; Sarkar, T.; Barucca, G.; Varvaro, G.; Locardi, F.; Peddis, D.; Mathieu, R. Tuning the magnetic properties of hard-soft SrFe$_{12}$O$_{19}$/CoFe$_2$O$_4$ nanostructures via composition/interphase coupling. *J. Phys. Chem. C* **2021**, *125*, 5927–5936. [CrossRef]
28. Omelyanchik, A.; Salvador, M.; D'orazio, F.; Mameli, V.; Cannas, C.; Fiorani, D.; Musinu, A.; Rivas, M.; Rodionova, V.; Varvaro, G.; et al. Magnetocrystalline and surface anisotropy in cofe2o4 nanoparticles. *Nanomaterials* **2020**, *10*, 1288. [CrossRef]
29. Dirba, I.; Schwöbel, C.A.; Zintler, A.; Komissinskiy, P.; Molina-Luna, L.; Gutfleisch, O. Production of Fe nanoparticles from γ-Fe$_2$O$_3$ by high-pressure hydrogen reduction. *Nanoscale Adv.* **2020**, *2*, 4777–4784. [CrossRef]

30. Aylmer, D.; Rowe, M.W. Effects of a strong external magnetic field on the reduction of cobalt and iron oxides: Confirmation. *J. Chem. Phys.* **1983**, *78*, 2094–2095. [CrossRef]

31. Chernavsky, P.A.; Kim, N.V.; Andrianov, V.A.; Perfiliev, Y.D.; Novakova, A.A.; Perov, N.S. The influence of an external magnetic field on the dynamics of magnetite reduction with hydrogen. *RSC Adv.* **2021**, *11*, 15422–15427. [CrossRef]

32. Cannas, C.; Falqui, A.; Musinu, A.; Peddis, D.; Piccaluga, G. $CoFe_2O_4$ nanocrystalline powders prepared by citrate-gel methods: Synthesis, structure and magnetic properties. *J. Nanoparticle Res.* **2006**, *8*, 255–267. [CrossRef]

33. Omelyanchik, A.; Levada, K.; Pshenichnikov, S.; Abdolrahim, M.; Baricic, M.; Kapitunova, A.; Galieva, A.; Sukhikh, S.; Astakhova, L.; Antipov, S.; et al. Green Synthesis of Co-Zn Spinel Ferrite Nanoparticles: Magnetic and Intrinsic Antimicrobial Properties. *Materials* **2020**, *13*, 5014. [CrossRef] [PubMed]

34. Omelyanchik, A.; Singh, G.; Volochaev, M.; Sokolov, A.; Rodionova, V.; Peddis, D. Tunable magnetic properties of Ni-doped $CoFe_2O_4$ nanoparticles prepared by the sol–gel citrate self-combustion method. *J. Magn. Magn. Mater.* **2019**, *476*, 387–391. [CrossRef]

35. Graulis, S.; Chateigner, D.; Downs, R.T.; Yokochi, A.F.T.; Quirós, M.; Lutterotti, L.; Manakova, E.; Butkus, J.; Moeck, P.; Le Bail, A. Crystallography Open Database—An open-access collection of crystal structures. *J. Appl. Crystallogr.* **2009**, *42*, 726–729. [CrossRef]

36. Holzwarth, U.; Gibson, N. The Scherrer equation versus the 'Debye—Scherrer equation'. *Nat. Nanotechnol.* **2011**, *6*, 534. [CrossRef]

37. Sandler, S.E.; Fellows, B.D.; Mefford, O.T.; Thompson Mefford, O. Best Practices for Characterization of Magnetic Nanoparticles for Biomedical Applications. *Anal. Chem.* **2019**, *91*, 14159–14169. [CrossRef]

38. Chernavskii, P.A.; Lunin, B.S.; Zakharyan, R.A.; Pankina, G.V.; Perov, N.S. Experimental setup for investigating topochemical transformations of ferromagnetic nanoparticles. *Instrum. Exp. Tech.* **2014**, *57*, 78–81. [CrossRef]

39. Vaitkus, A.; Merkys, A.; Gražulis, S. Validation of the Crystallography Open Database using the Crystallographic Information Framework. *J. Appl. Crystallogr.* **2021**, *54*, 661–672. [CrossRef]

40. Ferreira, T.A.S.; Waerenborgh, J.C.; Mendonça, M.H.R.M.; Nunes, M.R.; Costa, F.M. Structural and morphological characterization of $FeCo_2O_4$ and $CoFe_2O_4$ spinels prepared by a coprecipitation method. *Solid State Sci.* **2003**, *5*, 383–392. [CrossRef]

41. Dionne, G.F. *Magnetic Oxides*; Springer US: Boston, MA, USA, 2009; Volume 8, ISBN 978-1-4419-0053-1.

42. Demortière, A.; Panissod, P.; Pichon, B.P.; Pourroy, G.; Guillon, D.; Donnio, B.; Bégin-Colin, S. Size-dependent properties of magnetic iron oxide nanocrystals. *Nanoscale* **2011**, *3*, 225–232. [CrossRef]

43. Omelyanchik, A.; da Silva, F.G.; Gomide, G.; Kozenkov, I.; Depeyrot, J.; Aquino, R.; Campos, A.F.C.; Fiorani, D.; Peddis, D.; Rodionova, V.; et al. Effect of citric acid on the morpho-structural and magnetic properties of ultrasmall iron oxide nanoparticles. *J. Alloy. Compd.* **2021**, *883*, 160779. [CrossRef]

44. Knobel, M.; Nunes, W.C.; Socolovsky, L.M.; De Biasi, E.; Vargas, J.M.; Denardin, J.C. Superparamagnetism and other magnetic features in granular materials: A review on ideal and real systems. *J. Nanosci. Nanotechnol.* **2008**, *8*, 2836–2857. [CrossRef]

45. Jones, N.J.; McNerny, K.L.; Wise, A.T.; Sorescu, M.; McHenry, M.E.; Laughlin, D.E. Observations of oxidation mechanisms and kinetics in faceted FeCo magnetic nanoparticles. *J. Appl. Phys.* **2010**, *107*, 09A304. [CrossRef]

46. Nishizawa, T.; Ishida, K. The Co−Fe (Cobalt−Iron) system. *Bull. Alloy Phase Diagr.* **1984**, *5*, 250–259. [CrossRef]

47. Coey, J.M.D. *Magnetism and Magnetic Materials*; Cambrige University Press: New York, NY, USA, 2010; ISBN 0521816149.

48. Krishnan, K.M. *Fundamentals and Applications of Magnetic Materials*; Oxford University Press: Oxford, UK, 2016; ISBN 9780199570447.